RESEARCH

A DFT Study of Bandgap Engineering and Tuning of Structural, Electronic, Optical, Mechanical and Transport Properties of Novel [Ba$_4$Sb$_4$Se$_{11}$]: Sr^{3+} Selenoantimonate for Optoelectronic and Energy Exploitations

Kakul Husain[1] · Muhammad Irfan[2] · Sana Ullah Asif[3] · Mudassir Hussain Tahir[4,5]

Abstract

The comprehensive first-principles analysis of Ba$_4$Sb$_4$Se$_{11}$ and [Ba$_4$Sb$_4$Se$_{11}$]:Sr^{3+} Selenoantimonate Using DFT demonstrates its semiconductor nature, anisotropic ductile properties, and prospective optoelectronic applications, particularly in solar cells and LED technologies, supported by comprehensive structural, electronic, optical, and mechanical studies. All the relevant parameters were determined in this investigation using the framework of DFT by modified Becke Johnson approximations. These parameters include the extinction coefficient, absorption coefficient, energy loss function, reflectivity, refractive index, optical conductivity, and birefringes. The elastic parameters have been calculated based on anisotropic sound velocities and mechanical stability. These parameters include bulk modulus, shear modulus, Young's modulus, and Poisson's ratio. Based on an analysis of the energy band dispersions, it can be concluded that the examined compounds possess semiconductor properties. The data on elastic parameters suggest that the material exhibits anisotropic and ductile characteristics, which could have potential applications in optoelectronics. The Ba$_4$Sb$_4$Se$_{11}$ (2.2 eV) and [Ba$_4$Sb$_4$Se$_{11}$]: Sr^{3+} (1.68 eV) have a direct band gap, which falls within the visible spectrum showing semiconducting nature. The analysis of the thermoelectric properties of investigated compounds has been conducted using the Boltztrap code, marking a significant in scientific research. The study revealed that these compounds have the potential to be utilized in highly challenging transport conditions. Additional investigations and cooperation are essential for understanding the fundamental processes and enhancing the material for effective utilization in various technological applications for solar cells and LED in the energy and optoelectronic industry.

Keywords Band structure · Optical devices · Sustainable energy · SDG roadmap · Energy and industry · Technology

✉ Kakul Husain
  kakulhusain@gmail.com

✉ Sana Ullah Asif
  sanaullahasif@gmail.com

1   Department of Chemistry, College of Science and Humanities in Al-Kharj, Prince Sattam Bin Abdulaziz University, 11942 Al-Kharj, Saudi Arabia

2   Department of Physics, University of Sargodha, Sargodha 40100, Pakistan

3   School of Materials and Energy, Yunnan University, Kunming 650091, People's Republic of China

4   Research Faculty of Agriculture, Field Science Center for Northern Biosphere, Hokkaido University, Sapporo, Japan

5   School of Materials Science and Engineering, Tongji University, Shanghai 201804, China

1 Introduction

Structural and preparative studies show that anionic moieties of the alkali metal Selenoantimonate can take many forms. We use three primary components: tetrahedra of SbS$_3$, trigonal of SbS$_4$ tripyramids, and SbS$_5$ octahedral [1, 2]. On the other hand, information is known for sure on the structures of related compounds that contain higher concentrations of sulfur [3–5]. A compound with an unusual stoichiometry is Ba$_4$Sb$_4$Se$_{11}$ structure, in addition to Se's presence, such as distinct anionic Sb–Se ions, separated by 236.7 pm classes have been shown by complete X-ray crystal study of individual crystals bonds, bond angles, and bond lengths. Two distinct dinuclear Sb$_2$Se$_4$ units, which reflect the transfiguration of two SbSe$_3$ pyramids connected by a standard edge, are seen in addition to distorted trigonal SbSe$_3$ pyramids, also

known as tetrahedra [6, 7]. So far, in the structural chemistry of trivalent antimony compounds, this unusual connection has only ever resulted in tiny isolated units [8–10]. The term "selenoantimonate" has been used to describe compounds containing selenium and antimony.

Selenium and antimony have various compounds with potential uses in electronics, medicine, materials science, and other disciplines. The catalytic characteristics of selenium compounds may be enhanced by selenoantimonate, which contains both selenium and antimony. Because antimony compounds are frequently used in electronics and materials research, their presence also implies possible uses in these fields. Given selenium's well-deserved reputation as a vital trace element for human health, the biocompatibility of selenoantimonate raises the possibility of its use in therapeutics. Additionally, research into selenium compounds has focused on photovoltaic devices for use with solar energy [11, 12]. Importantly, selenoantimonate particular benefits would be contingent upon its distinct characteristics, necessitating additional study [13–15]. Recent scientific literature and study findings should be consulted for the most up-to-date and accurate information. Selenium (Se), barium (Ba), and antimony (Sb) have many uses and benefits in many different fields. Medical imaging relies heavily on barium because of its exceptional X-ray absorption properties, significantly improving diagnostic techniques. At the same time, antimony is used in flame retardants to make things safer, and it is an alloy to make other metals better. Photovoltaics, which use sun cells to generate electricity, rely heavily on selenium. Selenium isn't just functional for solar power; it is a vital trace element for human health, aiding in antioxidant defenses and immune function [16–18].

Furthermore, glass manufacturers utilize selenium compounds to enhance transparency [19, 20]. Taken as a whole, these components highlight their importance in boosting technology and people's health by demonstrating a wide array of contributions covering health, medical diagnostics, materials improvement, renewable energy, and more. A fascinating class of materials, Selenoantimonate has remarkable structural complexity and significant features such as photovoltaicity, photoelectricity, optical property, and luminescence property [21, 22]. The family of compounds, the $A_2M_2Q_5$ compounds, $Ba_5Ga_2S_8$, $Ba_4Ga_2S_7$, $Ba_3Ga_2S_6$, and $Mg_5Al_2Se_{11}$, are just a few of the ternary Chalcogenides, since 1970, a great deal of research has been done on the luminous characteristics of doping. It has been discovered that several of them have highly appealing luminescent features [23–27].

Salman et al. investigated the physical properties of the novel semiconductors $BaQCuS_3$ (Q = Er and Gd) by DFT calculations. Based on the analysis, it is observed that the compounds being studied have indirect band gaps in their predicted band structures. The predicted thermodynamic properties play a crucial role in determining the stability of these compounds. The results achieved in this study will significantly influence the development of efficient integrated optoelectronic devices and expand their range of practical applications [28–30]. Liu et al. investigate the phase stability, optoelectronic properties, and photovoltaic performance of $AHfX_3$ (A = Ca, Sr, Ba; X = S, Se) and their alloys. The optimized lattice parameters of $CaHfS_3$, $SrHfS_3$, and $BaHfS_3$ agree with the experimental data. Through the use of the screened hybrid functional HSE06, a detailed exploration has been conducted. The results indicate that the electronic band gaps of $SrHfS_3$ and $BaHfS_3$ have been accurately predicted. Additionally, it has been observed that the energy band gap of $AHfX_3$ can be tuned by alloying Se [31]. Extensive research was conducted on $CsZrCuSe_3$ to explore its electronic properties, which led to the discovery of a direct bandgap of 1.32 eV at the Γ point. An analysis was conducted on the optical properties, specifically the dielectric constant and optical conductivity, which revealed a significant absorption in the violet-blue range. The thermoelectric properties are of great interest in the scientific community. Interestingly, there is an anomaly in the Seebeck coefficient that is observed at specific chemical potentials. This anomaly offers a chance to understand better the intricate relationship between electronic properties in semiconductor materials [32–34].

Due to the novelty of $Ba_4Sb_4Se_{11}$ and $[Ba_4Sb_4Se_{11}]$, Sr^{3+} band structure computations must be investigated for optoelectronic industry applications. Transition metal chalcogenides have garnered significant interest due to their practicality, affordability, thermal stability, and impressive energy and power density. These properties are attributed to the alloy-conversion type used in metal-ion batteries, which sets them apart from the intercalation process of graphitic/graphene materials. In addition, metal transition chalcogenides exhibit a greater capacity for storing metal ions. Their significant redox activities enhance electrochemical properties compared to metal oxides. To obtain more precise predictions of electronic properties and energy gap values, we employ a different approximation called "TB-mBJ", which is the modified Becke-Johnson potential. To develop a cutting-edge electrode material based on transition metals, scientists must find a way to regulate the changes in volume expansion of the material. This is crucial to prevent the excessive clustering of sulfide, selenides, and phosphides, which can hinder conductivity. To address these challenges, materials derived from MOFs have provided a novel approach for creating materials that are highly porous, flexible, and capable of increasing the surface area of the desired material [35, 36]. In the field of sources like LEDs or lasers, one major challenge with silicon or SiGe is the indirect band structure, which results in very small optical transition matrix elements. Extensive research has been conducted

on emitters which involve Si/SiGe multi-quantum wells and ordered-strained layer Superlattices (SLS). Research has demonstrated through advanced calculations that the specific arrangement of the artificial lattice in ordered SLS can result in zone-folding within the Brillouin zone. Nevertheless, there is a lack of published research on the pressure-dependent comparisons of the elastic, mechanical, electronic, and optical characteristics of $Ba_4Sb_4Se_{11}$. The compound has significant advantages for optoelectronic devices due to its ability to adjust the band gap. This adjustment enhances the movement of electrons from the valence band to the conduction band, resulting in improved optical absorption and conductivity. The calculation involves more than financial costs, and effective intervention yields good consequences. Process speed is high, while computational resources are modest. We use first-principles global structural optimization to evaluate their solar photovoltaic suitability [37–40].

2 Computational Details

Within a self-consistent methodology, we evaluated the optical, electrical, and structural characteristics of tetragonal $Ba_4Sb_4Se_{11}$ and $[Ba_4Sb_4Se_{11}]$: Sr^{3+} structures by solving the Kohn–Sham equation using basic principles. We used the PBE (Perdew Burke Ernzerhof) for structural optimization. The electrical and optical computations were performed using the Wien2k code's modified Becke–Johnson potential (mBJ) [41] to achieve more precise findings. The FP-LAPW approach, which stands for self-consistent full potential linearized augmented plane wave, was used for all computations [40, 42]. The interstitial region (muffin-tin) spheres comprise the unit cell. Harmonic functions are primarily within the (MT) and the interstitial region. For Ba, Sb, Se, and Sr, the MT sphere radii are selected correspondingly as 2.20, 2.40, 2.98, 1.75, and 1.15 a.u. We settled on -7 Ry as the energy of the split between the core and valence states. With a cutoff value $R_{mt}K_{max} = 8$, we can see that the basis set has converged; here, Kmax is the most significant mutual lattice vector utilized in the plane wave dilation, and R_{mt} is the minor MT sphere radius. The maximum charge density Fourier expansion vector's magnitude (G_{max}) was 12. We choose 0.0001 as the energy convergence criterion. The convergence threshold for a charge during self-consistency cycles (SCF) is 0.0001e; in each self-consistency phase, the charge density was determined by integrating over the (BZ). This technique used 150 specific k-points in the irreducible zone containing 2000 k-points in the complete BZ.

To obtain more precise predictions of electronic properties and energy gap values, we employ an alternative approximation called "TB-mBJ", which is the modified Becke-Johnson potential [43]. This approach yields results that are in better alignment with experimental data. In the

FP-LAPW method, the unit cell is divided into two distinct regions. The first region consists of non-overlapping spheres centered on each atom, commonly called Muffin-tin spheres. These spheres have a specific radius, denoted as RMT. The second region is known as the interstitial region. Calculations are performed using a self-consistent field geometry to determine wave functions, electronic densities, and potentials. By manipulating factors such as the composition of Sr, it is possible to alter the electronic and optical properties of these materials. Additionally, the optical absorption coefficient increases, and the absorption spectrum shifts towards longer wavelengths, resulting in a redshift. Through the manipulation of strain and variations in composition, it is possible to adjust the optical absorption spectrum to meet specific requirements precisely, covering a wide range from visible to ultraviolet range. Optoelectronic transmitters and receivers are connected to digital logic through advanced amplifiers explicitly designed for this purpose. Although the drivers generate a significant amount of heat and many optoelectronic parts are sensitive to high temperatures, there is a strong drive to achieve greater levels of integration. This is especially true in the fast-evolving realm of silicon photonics. Extensive research has been conducted on monolithic integration, focusing on the requirements of optical waveguides.

The Tran and Blaha approach builds upon the research conducted by Becke and Johnson. Straightforward and efficient potential for exchange has been suggested, which primarily relies on the overall density and the kinetic energy density as described in equation.

$$V_{X,\sigma}^{mBJ}(r) = V_{X,\sigma}^{Slater}(r) + \Delta V_{X,\sigma} = V_{X,\sigma}^{Slater}(r) + \frac{1}{\pi}\sqrt{\frac{5}{12}}\sqrt{\frac{t}{\rho}}$$

(1)

$\Delta V_{X,\sigma} = \frac{1}{\pi}\sqrt{\frac{5}{12}}\sqrt{\frac{t}{\rho}}$ The difference between the optimized elective potential proposed by Krieger et al. [11] and the Slater potential can be examined. The optical dielectric constants were calculated using the random phase approximation (RPA), as implemented by Ambrosch-Draxl and Sofo [25] in the Wien2k code. The optical parameters are expressed as $\alpha(\omega)$, $\varepsilon_1(\omega)$, $\varepsilon_2(\omega)$, $R(\omega)$, $n(\omega)$, $k(\omega)$ The optical absorption coefficient plays a crucial role in determining the performance characteristics of solar cells.

$$\alpha(\omega) = \sqrt{2}\omega\left[\left\{\varepsilon_1^2(\omega) + \varepsilon_2^2(\omega)\right\}^{1/2} - \varepsilon_1(\omega)\right]^{1/2}$$

(2)

The system's reaction to an external electromagnetic field with a slight wave vector is measured by examining the complex dielectric function. We will focus on frequencies that are significantly higher than those associated with phonons, allowing us to examine electronic excitations solely. The phenomenon of lifetime broadening can be accounted for by

convoluting the absorptive part with a Lorentzian function. The value of real and imaginary parts of complex dielectric function is given as

$$\varepsilon_1(\omega) = 1 + \frac{2}{\pi} P \int_0^\infty \frac{\varepsilon_2(\omega')\omega' d\omega'}{\omega'^2 - \omega^2} \tag{3}$$

$$\varepsilon_2^{ij}(\omega) = \frac{4\pi^2 e^2}{Vm^2\omega^2} \times \sum_{knn'\sigma} \langle kn\sigma|p_i|kn'\sigma\rangle \langle kn'\sigma|p_j|kn\sigma\rangle \\ \times f_{kn}(1 - f_{kn'})\sigma(E_{kn'} - E_{kn} - \hbar\omega) \tag{4}$$

Now, all-optical constants can be derived from this. Assuming that the crystal surface is parallel to the optical axis, we can determine the reflectivity using the formula.

$$R(\omega) = \left|\frac{N-1}{N+1}\right|^2 = \frac{(n-1)^2 + K}{(n+1)^2 + K} \tag{5}$$

here are the expressions for the extinction coefficient, and the refractive index is given as:

$$n(\omega) = \left[\frac{\sqrt{\varepsilon_1^2(\omega) + \varepsilon_2^2(\omega)}}{2} + \frac{\varepsilon_1(\omega)}{2}\right]^{1/2} \tag{6}$$

$$k(\omega) = \left[\frac{\sqrt{\varepsilon_1^2(\omega) + \varepsilon_2^2(\omega)}}{2} - \frac{\varepsilon_1(\omega)}{2}\right]^{\frac{1}{2}} \tag{7}$$

2.1 Structural and Thermodynamic Stability

First, we examine the $Ba_4Sb_4Se_{11}$ structural characteristics; the atomic positions and lattice constants are employed as initial values to find the ground state parameters. The structural optimization was done by computing the total energy for various c/a and b/a ratios using the Murnaghan equation of state [44, 45]. This allowed us to fix the values of these two parameters. By reducing the total amount of energy and the stresses exerted on each atom in the system, the locations of the atoms are found, and acquired data are shown together in Table 1. The estimated Ba–Sb bond length is also 2.443 Å, marginally more extended than the Ba–Se bond

length of 2.336 Å. This difference may be due to the size of the Se atom. Both the Ba–Ba and Se–Ba distances in BaSe are slightly more significant than their comparable ones in Ba-Sb–Se, which are 3.165 Å and 2.285 Å. On the other hand, we discovered that Ba-Sb–Se have bond lengths of 2.193 Å and 2.177 Å, respectively.

$$E(V) = E_0 + \left[\frac{\left(\frac{V_0}{V}\right)^{B_0'}}{B_0' - 1} + 1\right] - \frac{B_0 V_0}{B_0 - 1} \tag{8}$$

The formation energy, which may be used to verify the thermodynamic stability of all the materials tested, can be determined using the following equation [46].

$$E_{for} = \frac{[E_{Ba4Sb4Se11} - (AE_{Ba} + BE_{Sb} + CE_{Se}]}{A + B + C} \tag{9}$$

The first term in their ground state energy for investigated materials is the sum of the parent and doped materials' energies. The remaining terms total atomic energies in their most stable phase. The symmetric and optimized crystal structure is shown in Figs. 1 and 2.

2.2 Electronic Properties

The band configuration specifically designated the energy that electrons can generate through the diffusion of dynamical electrons inside a crystal lattice. Its band structure shows its physical characteristics, including its optoelectronic properties. Figure 3 compares the band structures computed for $Ba_4Sb_4Se_{11}$ and $[Ba_4Sb_4Se_{11}]$: Sr^{3+} simultaneously. Since the VBM and the CBM are situated at the high symmetry point, both materials display the properties associated with direct band gap semiconductors. Additionally, the band diagram illustrates a vertical transition direction for the electronic guide band transitions that occur in the valence band. With this information, we may deduce that the momentum of the electrons in $Ba_4Sb_4Se_{11}$ does not undergo any changes throughout the phase transition.

On the other hand, if the electrons are moved to the VB while the rate remains the same, there is a greater possibility of electron and hole recombination. This investigated material is a material that has the potential to be effective

Table 1 Calculated lattice parameters ratio, bulk modulus (B_0) GPa and its pressure derivative B', formation energy E_{for} (eV/cell), internal parameter (u_0), $Ba_4Sb_4Se_{11}$ and $[Ba_4Sb_4Se_{11}]$: Sr^{3+} selenoantimonate

Compound	a	b	c	c/a	b/a	B(GPa)	B'	E_{for}(eV/cell)	u_0
$Ba_4Sb_4Se_{11}$	10.35	9.81	12.25	1.18	0.94	330	9.9	− 5.04	0.45
$Ba_4Sb_4Se_{11}$: Sr^{3+}	11.89	9.97	14.98	1.25	0.83	458	8.32	− 2.99	0.84

Fig. 1 a–d Symmetric crystal structures of $Ba_4Sb_4Se_{11}$ and $[Ba_4Sb_4Se_{11}]$: Sr^{3+} Selenoantimonate
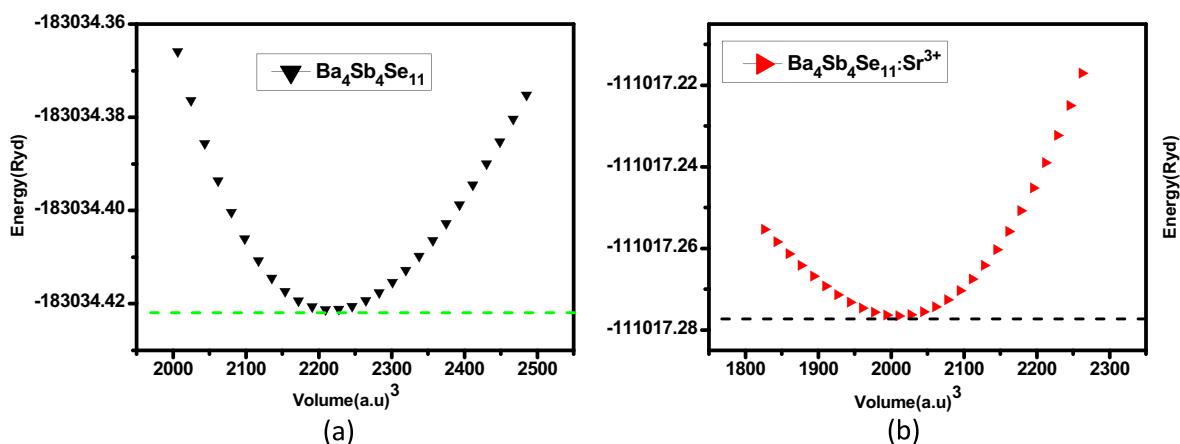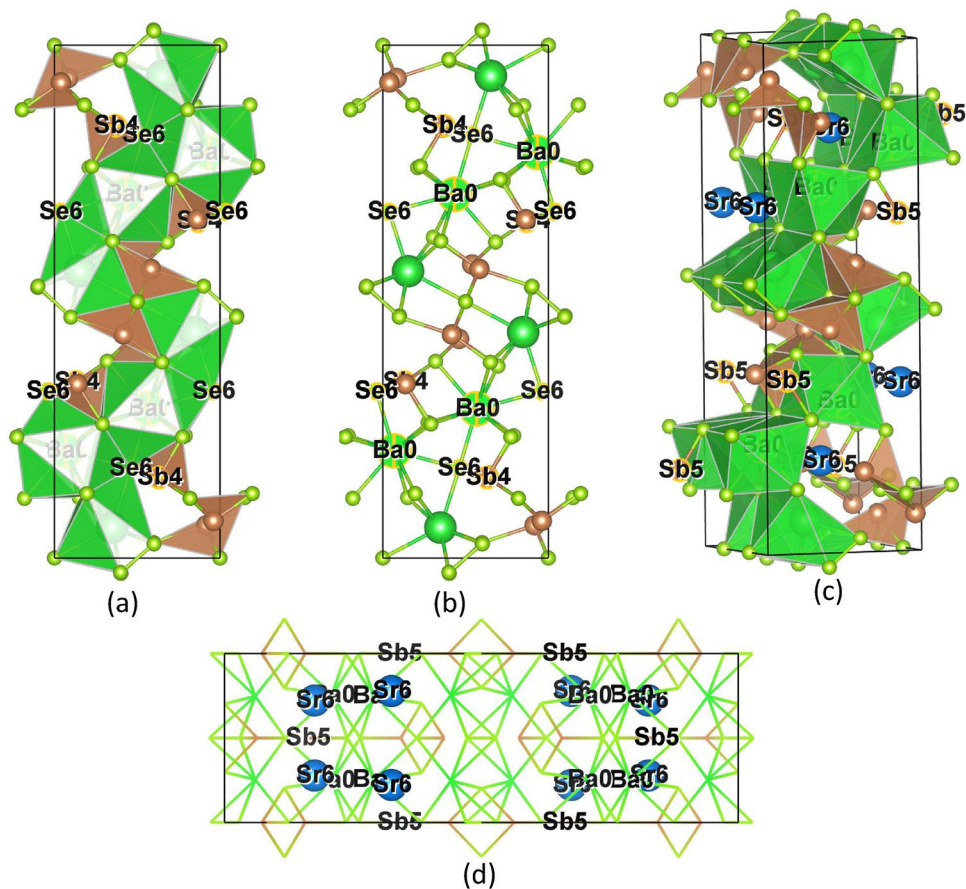
Fig. 2 The volume optimization plots of $Ba_4Sb_4Se_{11}$ and $[Ba_4Sb_4Se_{11}]$: Sr^{3+} Selenoantimonate by Murnaghan equation of state

in optical switches due to the significantly short carrier lifetime that it usually possesses. As a result of the majority of energy being released as visible light, this technique is highly effective. The band structure makes the fact that both processes are utilized in producing luminous components abundantly clear. As the band gap widens, the increase in the electron's ability to be excited is accompanied by a

decrease in the carrier concentration and conductivity. The investigation is demonstrated by the band gap between bulk $Ba_4Sb_4Se_{11}$ and $[Ba_4Sb_4Se_{11}]$: Sr^{3+} is 2.2 and 1.6 eV, respectively, which was found by first-principles calculation. This band gap type is consistent with our investigated materials because of their narrow band gap and significant absorption of the visible and near-infrared spectrums; all parental
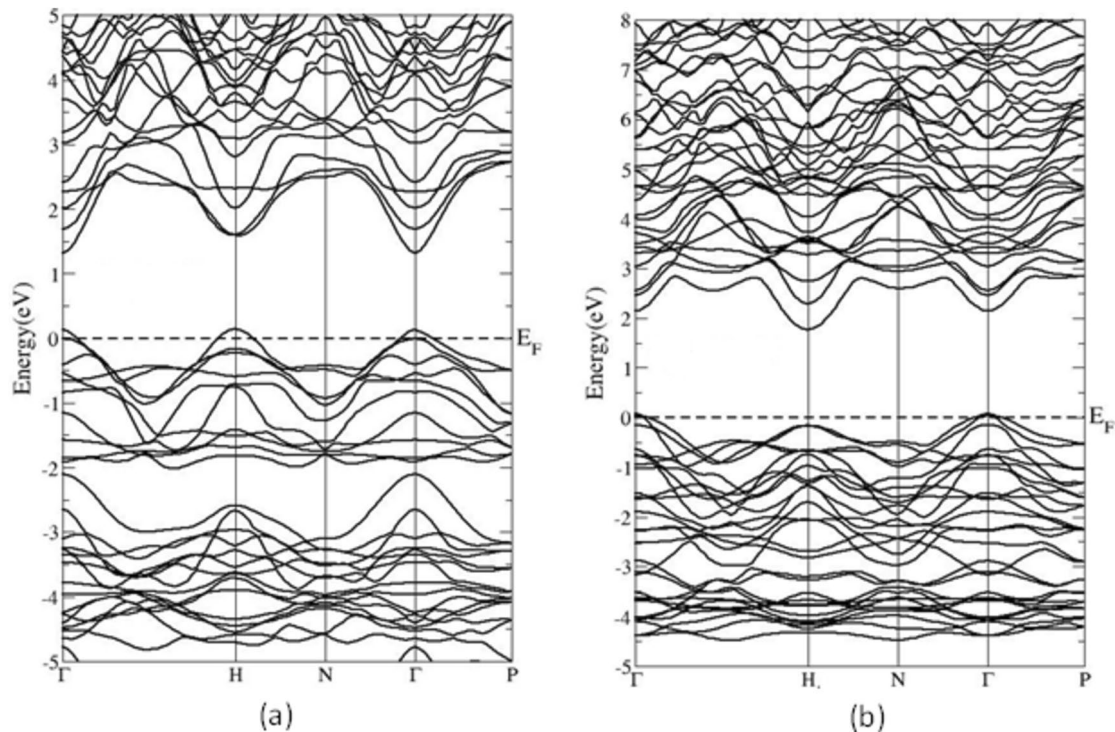
Fig. 3 Calculated energy band structures of $Ba_4Sb_4Se_{11}$ and $[Ba_4Sb_4Se_{11}]$: Sr^{3+} Selenoantimonate by modified Becke Johnson (mBJ) approximations

and doped compounds are ideally suited for photoelectronic applications [47]. The computed direct band gap is 2.18 eV, which reasonably agrees with the experimental result from the diffuse reflectance spectrum. The results did not alter if other pseudo-potentials were utilized for the calculations [48]. The semiconducting industry relies heavily on the density of states (DOS) of different thicknesses of crystals as a reflection of their chemical bonding mechanisms. Figure 4 and 5 show all examined materials' TDOS and partial PDOS to explore the chemical bonding mechanism of $Ba_4Sb_4Se_{11}$ and $[Ba_4Sb_4Se_{11}]$: Sr^{3+}.

Additionally, a flat line representing the Fermi level is set to zero. The peaks and characteristics of DOS of the $Ba_4Sb_4Se_{11}$ and $[Ba_4Sb_4Se_{11}]$: Sr^{3+} are distinctly similar and have particular characteristics. First, Se-s, p /Ba-p, and Se-d electronic states predominate at valence bands for the parental compound. Second, the conduction band is segmented with Ba-d/Se-s/Sb-s electron states. The doped material $[Ba_4Sb_4Se_{11}]$: Sr^{3+} significantly affects the valence band and conduction band by different electronic states. The valence band is formed with Sb-s/Se-p/Ba-p and Se/Ba-d orbitals, while Ba-/Se-d mainly originated in CB. The Ba-d and Se-d contributed to the top of the conduction band more than the Se/Sb/Sr/Ba-s-p electronic states. The primary bonding electrons are incorporated into the lower energy region, with the overall (DOS) between -8.0 eV and 8.0 eV. This indicates

that they only serve to compensate for the charge valence and do not directly influence the band edge states. It suggests that the optoelectronic properties of Selenoantimonate compression of the Ba–S/Se bond resulted in a stronger connection between the different orbitals. This led to an elevation of the VBM and increased band dispersion. The CBM did not exhibit a response to pressure while it was predominantly in a nonbonding localized state. Through increasing the VBM, the strengthened orbital coupling resulted in a decrease in the band gap.

3 Optical Properties

The behavior of materials when interacting with light is described by their optical properties. This includes how they absorb, reflect, transmit, and emit electromagnetic radiation in the visible, ultraviolet, and infrared regions of the electromagnetic spectrum. These characteristics offer valuable information about the way materials interact with light and are crucial for a wide range of applications in fields like optoelectronics, photonics, and materials science. Its electronic band structure mainly determines the properties of a material. The percentage of energy an item absorbs for every unit of light that travels through it is referred to as the absorption coefficient [49]. While a substance's sort usually

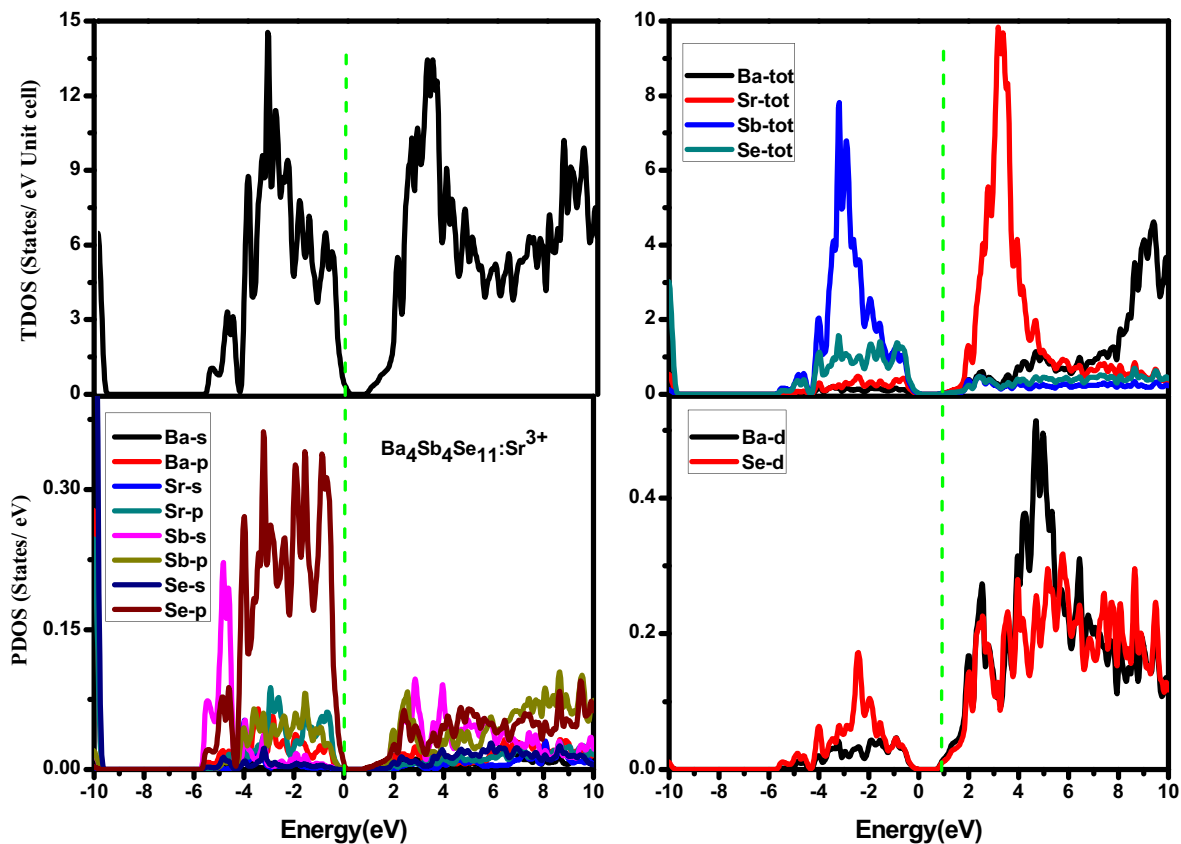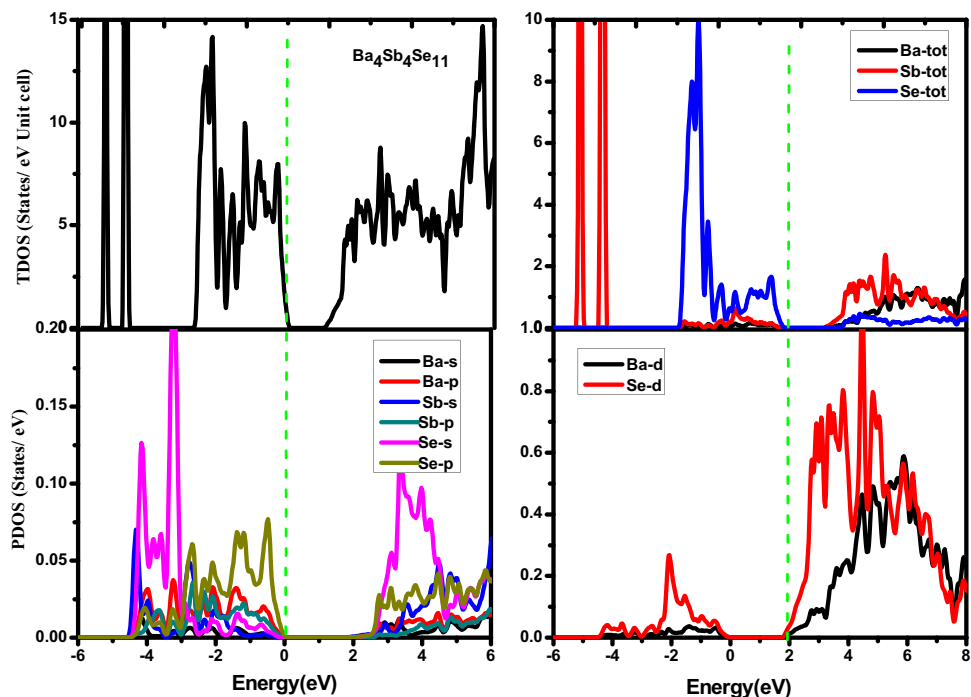**Fig. 4** Calculated and total and partial densities of states (T/PDOS) of $Ba_4Sb_4Se_{11}$ Seleno-antimonate

Fig. 5 Calculated and total and partial densities of states (T/PDOS) of $[Ba_4Sb_4Se_{11}]$: Sr^{3+} Selenoantimonate

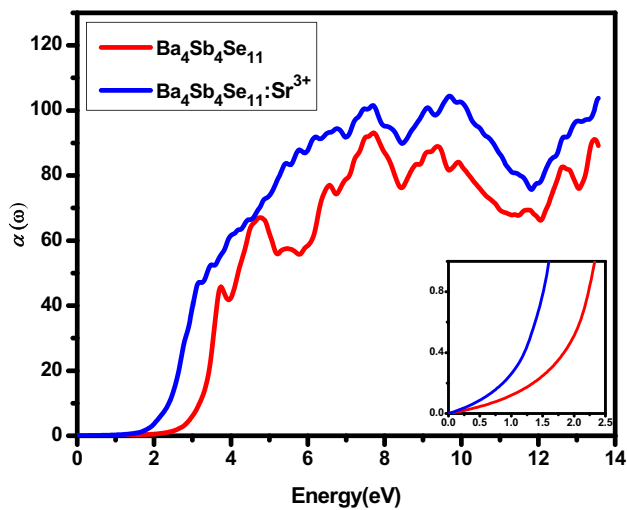**Fig. 6** Variation of absorption coefficient with energy of $Ba_4Sb_4Se_{11}$ and $[Ba_4Sb_4Se_{11}]$: Sr^{3+} Selenoantimonate

Fig. 7 Variation of optical conductivity with energy of $Ba_4Sb_4Se_{11}$ and $[Ba_4Sb_4Se_{11}]$: Sr^{3+} Selenoantimonate

determines its absorption coefficient, structural differences within the same material can also impact it. Figure 6 shows absorption coefficients for $Ba_4Sb_4Se_{11}$ and $[Ba_4Sb_4Se_{11}]$: Sr^{3+}; it is observed that critical values of absorption occur at 2.1 eV and 1.8 eV, respectively. The region of maximum absorption is located around − 0.4–10 eV for both investigated compounds. The crystal's infrared absorption capability demonstrates its semiconducting nature with increased hydrogen effects in the doped scenario. Therefore, it would be preferable to use Sr-doped crystal orientation while making infrared photoelectric detectors. Bulk material is a fantastic alternative for UV and visible light detectors since parental compounds have a considerable capacity for light absorption in these wavelength ranges.

Optical conductivity can be calculated by adding real and imaginary components [50].

$$\sigma(\omega) = \sigma_1(\omega) + \sigma_2(\omega) \tag{10}$$

Optical conductivity represents free charge carrier conduction computed using the VB-CB transitions of dielectric functions. The optical conductivity of the examined material is displayed in Fig. 7. Excitonic events are incapable of carrying charge and are created when energy exceeds the bandgap. Excitonic characteristics are present in all examined substances in the 4, 5, 6, and 7.2 eV range. For $Ba_4Sb_4Se_{11}$ and $[Ba_4Sb_4Se_{11}]$: Sr^{3+} at gamma points, the first transition can also be shown using the modified Becke Johnson (mBJ) approximation. Electronic transition-driven plasma excitations are responsible for optical conduction peaks. Below 1.8 eV, optical conductivity is minimal in both compounds; Sr doping boosts optical conductivity in the low-energy domain and peaks at 3.0 eV, 4.03 eV, 7.06 eV, and 9.33 eV
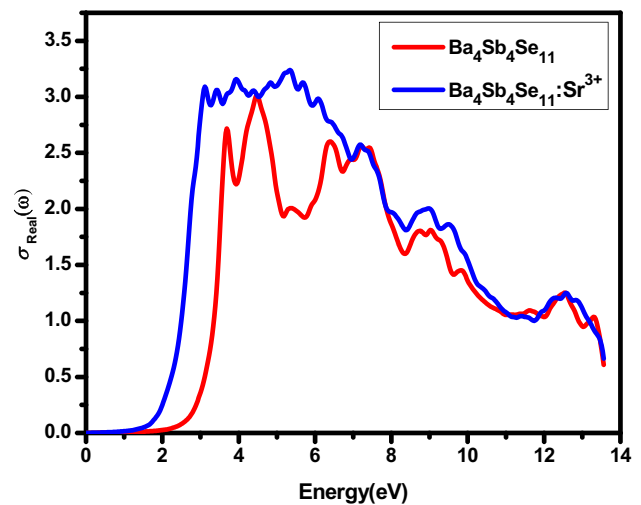
because of photon absorption. Comprehending the characteristics of optical conductivity that exhibit more significant peaks in the violet-blue spectrum is imperative when developing and refining apparatuses, substances, or frameworks that depend on interactions between light and matter, like photovoltaics, photodetectors, or optical filters. It was observed that both compounds exhibited higher absorption and photoconductivity. When analyzing the photoconductivity of these materials, it was observed that there were distinct peaks across a broad range of the energy spectrum.

The materials' responses to electric field stimulation are used to investigate the dielectric properties of crystals [51]. It is essential to talk about dynamic dielectric because of its strong correlation with the measurement frequency. Understanding the relationship between the material's dielectric constant and frequency when exposed to the electromagnetic field requires understanding the $Ba_4Sb_4Se_{11}$ and $[Ba_4Sb_4Se_{11}]$: Sr^{3+} dielectric function. The complex dielectric function and the optical characteristics usually represent additional attributes. The $\varepsilon(\omega)$ is obtained using the formula below: The dielectric constant and the refractive index's real and imaginary components. Based on the band structure, the dielectric function's estimated real $\varepsilon_1(\omega)$ and imaginary $\varepsilon_2(\omega)$ are shown in Figs. 8 and 9. By linking the state of the ultimate value of the imaginary part, it is simple to ascertain that the $Ba_4Sb_4Se_{11}$ and $[Ba_4Sb_4Se_{11}]$: Sr^{3+} of the bulk structure of a crystal orientation are the same.

On the other hand, the $[Ba_4Sb_4Se_{11}]$: Sr^{3+} undergoes a significant alteration and a blue shift. We examine the transitions to these peaks, considering the transitions. The prominent peaks in the dielectric function for all three forms of investigated material are caused by the transition between different orbitals to VB-CB. The figure shows that
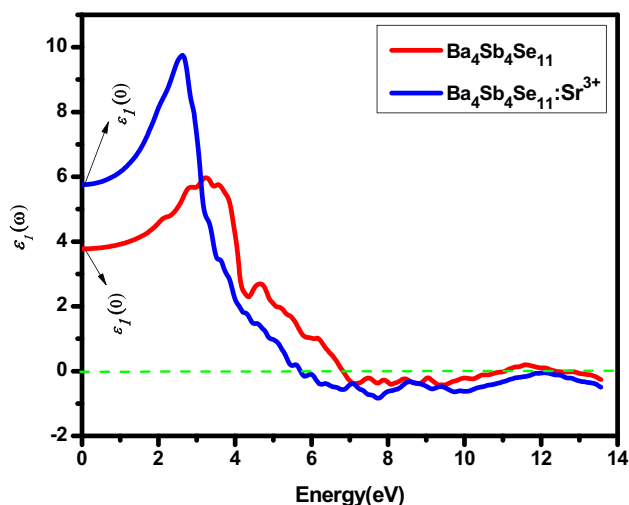
Fig. 8 Variation of real part of dielectric function with energy of $Ba_4Sb_4Se_{11}$ and $[Ba_4Sb_4Se_{11}]$: Sr^{3+} Selenoantimonate
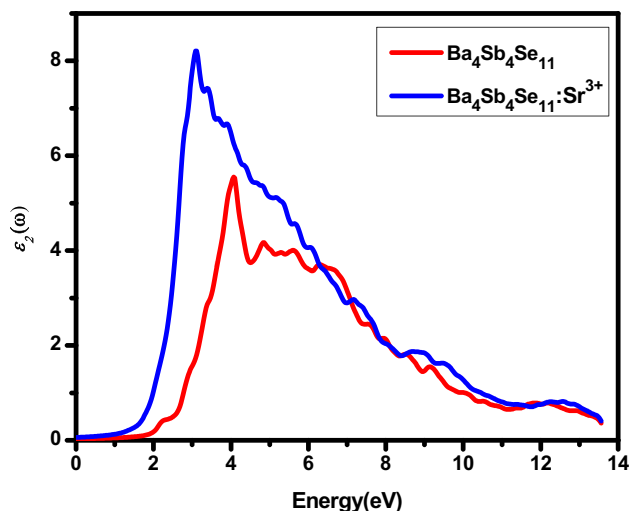
Fig. 9 Variation of the imaginary part of dielectric function with energy of $Ba_4Sb_4Se_{11}$ and $[Ba_4Sb_4Se_{11}]$: Sr^{3+} Selenoantimonate

the maximum dispersion occurred between 1.8–3.8 eV for both investigated materials. It was clear that there was a relationship between the imaginary part of the dielectric function and the optical absorption/transition, as well as the band gap of the material. It was observed that the imaginary part of the dielectric function caused the peaks to shift towards lower incident photon energy. This trend was consistent with the optical absorption shown in Fig. 8.

In contrast, the imaginary part of the dielectric function reached zero in the higher photon energy region. The kind of material and its electrical structure determine how the dielectric constant behaves close to the absorption edge. The dielectric constant exhibits a dramatic increase in the band

gap energy indirect band gap materials, where the valence band maximum and the conduction band minimum occur at the same momentum point in the Brillouin zone.

$$\varepsilon(\omega) = \varepsilon_1(\omega) + i\varepsilon_2(\omega) \qquad (11)$$

It is the ratio of the intensity of light reflected from the surface to the power of the light that is incident, referred to as the reflection coefficient [52]. The incident angle, the incident light's intensity, and the material's surface affect the object's reflection coefficient. Understanding the optical qualities requires analyzing the reflection coefficients of two materials, $Ba_4Sb_4Se_{11}$ and $[Ba_4Sb_4Se_{11}]$: Sr^{3+}. Figure 10 shows the examined reflectance coefficient spectra. Bulk $Ba_4Sb_4Se_{11}$ are widely used as photocatalysts due to their vital light absorption regions in the ultraviolet and visible light spectrum. Photoelectric devices can also take advantage of these materials. Bulk $Ba_4Sb_4Se_{11}$ and $[Ba_4Sb_4Se_{11}]$: Sr^{3+} have the most significant reflection coefficient values. Measurements are made of the wavelengths at which the reflection coefficient is highest, 13 eV and 11.9 eV for both parental and doped compounds. The more gradually the reflection coefficient falls below 3.0 eV, the more significant it is. While the doped $Ba_4Sb_4Se_{11}$ finally tends to be 2.49, the bulk tends to be between 10 and 18%. The bulk parental compounds' reflection coefficients are higher than the doped compounds', indicating that the reflection coefficients of the former are more significant in the visible and ultraviolet spectrums. As a result, both materials work well as an antireflective layer of the three constructions of these changes in crystal structure lead to altered electrical design and distinct atom-to-atom interactions. Theoretical calculations indicate that the ionic bond between the Ba and Sr atoms in
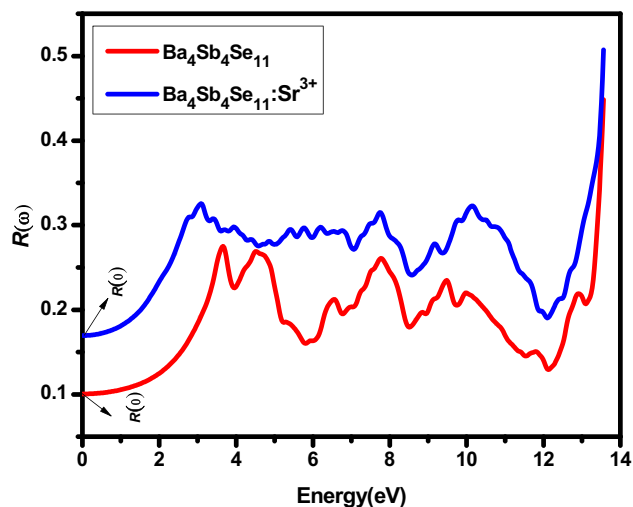

Fig. 10 Variation of optical reflectivity with energy of $Ba_4Sb_4Se_{11}$ and $[Ba_4Sb_4Se_{11}]$: Sr^{3+} Selenoantimonate

the molecules under investigation is more important. These findings may be helpful for novel Sr-based energy materials. By analyzing the reflectivity, it becomes evident that both investigated materials exhibit consistent responses across a broad range of energies in the ultraviolet region. With the application, there was a noticeable increase in the values of reflectivity and loss function in the UV region.

Electrons lose energy as they travel through a material; this phenomenon is described by the "energy loss" $L(\omega)$ [53]. Plasmonic oscillations cause the peaks, and $L(\omega)$ has a unique reaction. During the performance, plasmonic oscillations are produced by atomic cores equivocating against valence states. Plotting reveals that $L(\omega)$ peaked in the upper UV–visible region up to 6 eV. This suggests that the substance loses more energy and absorbs light more intensely. In other places, when electrons are driven into the (CB), the (BG) absorption rises, promoting electronic transitions and raising light absorption. The calculated energy loss curve for rapid electron loss is displayed in Fig. 6. Anisotropy in the UV and isotropy in the VB are shown in Fig. 11. Dominant plasmon oscillations from (VBM) and (CBM) at 13.0 eV were seen in all examined materials. Additionally, the figure shows that at 0–1.8 and 0–2.2 eV, $Ba_4Sb_4Se_{11}$ and $[Ba_4Sb_4Se_{11}]$: Sr^{3+} do not lose any energy. The most significant values of the energy loss function are 0.75, 0.65, and 0.3, which cause a sharp drop in reflectance, as shown in Fig. 8.

Its refractive index is how much light may flow in a material [54]. Use the dielectric function $n(\omega)$ to get the refractive index. The expressive refractive index in the (Vis-IR) regions determines the material's transparency and dispersion. A declining refractive index at specific energies indicates a reduction in the ability of light to be refracted. This

pattern is described by absorption bands in optical response. $Ba_4Sb_4Se_{11}$ and $[Ba_4Sb_4Se_{11}]$: Sr^{3+} exhibits a stronger absorption of light at 8 eV, as evidenced by its decrease in refractive index. The material's refractive index is lowered by absorbing light at an energy inside the absorption band. As was already noted, absorption peaks correspond to energy ranges. The more a substance absorbs, the lower its refractive index variations. Variations in refractive index can facilitate understanding of optical device architecture. The decrease in intensity shows that the speed of the input photon is less than the group velocity in opposition to the polarization. Sr-doped material has a more excellent static value than the parent compound. With an increase in energy (or light frequency), the $n(\omega)$ decreases significantly. The effect of photon energy on the refractive index is illustrated in Fig. 12. Atomic interactions at the atomic scale determine the refractive index of optical materials. Recognition of the band structure-dielectric function relationship is made. The refractive index of various materials can change based on the wavelength of light under consideration. Optoelectronic applications such as lenses, light guiding, antireflection coatings, photonic devices, waveguides, and metamaterials with customized optical properties are made possible by high refractive index in the visible range. The imaginary component of the index of refraction explains light absorption or attenuation through a substance. It shows the degree to which a material absorbs light at a specific wavelength. More excellent light absorption is seen in materials with higher extinction coefficients. The imagined part's presence impacts the transmission in optoelectronic applications.

$Ba_4Sb_4Se_{11}$ raised the static refractive index and $[Ba_4Sb_4Se_{11}]$: Sr^{3+}, as shown in Fig. 13. It is thought that phonons are neglected when dielectric screening is done.

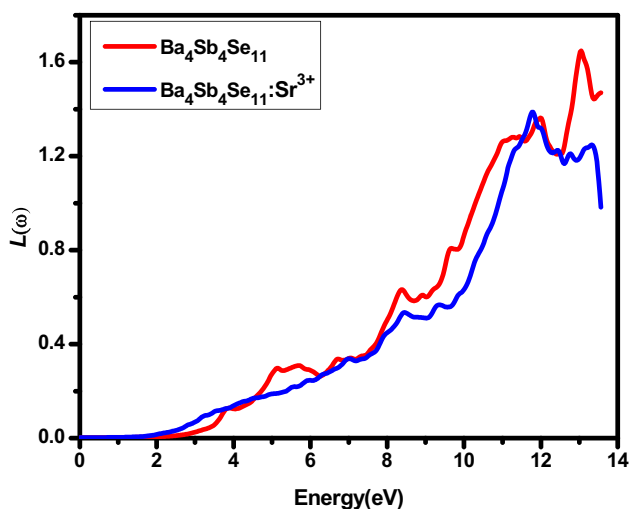**Fig. 11** Variation of energy loss function of $Ba_4Sb_4Se_{11}$ and $[Ba_4Sb_4Se_{11}]$: Sr^{3+} Selenoantimonate
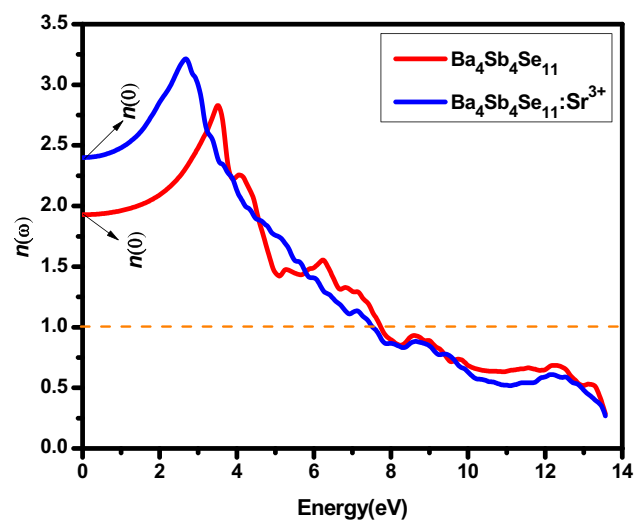
Fig. 12 Variation of refractive index with energy of $Ba_4Sb_4Se_{11}$ and $[Ba_4Sb_4Se_{11}]$: Sr^{3+} Selenoantimonate
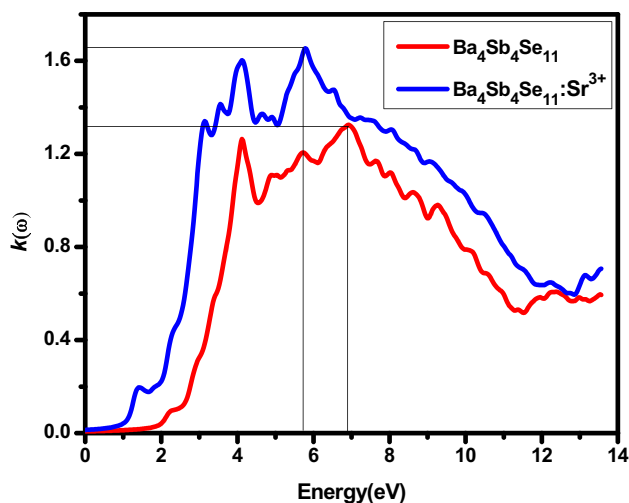
Fig. 13 Variation of extinction coefficient with energy of $Ba_4Sb_4Se_{11}$ and $[Ba_4Sb_4Se_{11}]$: Sr^{3+} Selenoantimonate

Static refractive index for the two materials under investigation, Sr-doped 2.4 and 1.8. The measurements show a few peaks at energies in the IR-UV region. The extinction coefficient, k (ω), exhibits properties of the investigated substance that can be understood as light absorption based on the extinction coefficient [55]. The value of k (ω) is one characteristic of its spectrum that sets it apart. Materials require photon absorption since photon transmission is absent below 0 eV. The material absorbs photons rather than emitting them. Significant peaks at 4–6 eV at specific energies indicate that the compounds consist of absorption bands linked to electronic transitions. Because the material's band structure links absorption peaks to particular energy levels or electronic states, photons can excite electrons, causing them to depart the VB-CB. Material bandgap and energy gap have an impact on peak energies. One must comprehend the visible spectrum's absorption qualities and peak positions to use optical sensors and light-emitting devices effectively. They are relevant since the examined material absorption peaks can impact them.

A remarkable phenomenon resulting from light deflection in two directions is exhibited by the double reflection, also known as birefringes [56]. When light travels in one of the available directions, its speed varies. Optical effects are used in microscopy and telecommunications in some material science domains. For $Ba_4Sb_4Se_{11}$ and $[Ba_4Sb_4Se_{11}]$: Sr^{3+}. Birefringes calculations were performed at zero frequency. The current work analyzed Δn (ω) for each tested material by minimizing the initial and final electron count. Birefringence in a non-absorbing media has become much more critical at energy levels below the energy band gaps. The significant spectrum variation resulting from the alteration in the total birefringes throughout the whole energy

spectrum is illustrated in Fig. 9. It was discovered that the low-frequency limit, represented by the symbol n (0), was − 0.140 for the Sr-doped compound and − 0.148 for the original compound, as indicated in Fig. 14. Because of this, every molecule under study exhibits a unique collection of phase-matching skills. Phase matching is guaranteed by the enormous magnitude of the birefringence over a wide frequency range. The non-absorbing region below the energy gap is the birefringes, which is significant because the band structures are identical (Table 2).

4 Mechanical Properties

Using first-principles calculations and the IR-Elast package [56], a comprehensive analysis was conducted to determine the mechanical properties of both compounds. The elastic constants play a vital and intriguing role in determining the physical properties of solid materials, as they dictate how a crystal responds to external forces. The elastic properties encompass its ability to experience stress, deform, recover, and revert to its initial shape [57]. These properties are essential in elucidating the binding between atomic planes and structural stability. The elastic constants are the connection between the mechanical and dynamic of crystals and offer stability requirements for a tetragonal material that can also be used to predict the structural stability of materials. The orthorhombic is characterized by nine elastic constants, specifically C_{11}, C_{22}, C_{33}, C_{44}, C_{55}, C_{66}, C_{12}, C_{13}, and C_{23} [58]. The elastic constants of ten orthorhombic compounds were determined using the ortho-elastic package and are presented in Table 3. Both $Ba_4Sb_4Se_{11}$ and $[Ba_4Sb_4Se_{11}]$: Sr^{3+} can enhance their mechanical stability by determining their
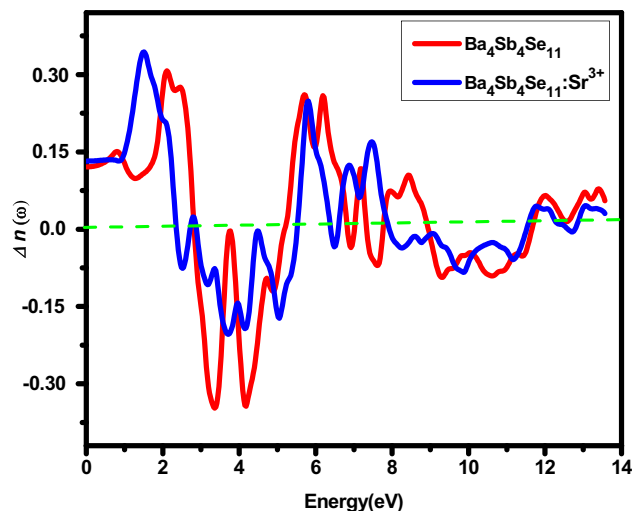
Fig. 14 Variation of Birefringes of $Ba_4Sb_4Se_{11}$ and $[Ba_4Sb_4Se_{11}]$: Sr^{3+} Selenoantimonate

Table 2 Calculated optical energy band gap, dielectric function, refractive index, and plasmon energy of $Ba_4Sb_4Se_{11}$ and $[Ba_4Sb_4Se_{11}]$: Sr^{3+}

Compounds	E_g (eV)	$\varepsilon_1(0)$	$n(0)$	$\sigma(\omega)$	$R(0)$	$\Delta n(0)$
$Ba_4Sb_4Se_{11}$	2.2	3.4	2.1	6.0	0.14	0.140
$[Ba_4Sb_4Se_{11}]$: Sr^{3+}	1.6	4.1	2.4	7.0	0.16	0.148

structural properties and establishing their energetic stability through formation energy analysis. The elastic property is a good choice for this case and performs well in achieving this goal. It is possible to use this model to estimate the constants (C_{ij}), which determines how well they satisfy the requirements for mechanical stability. The following equations are used to calculate the mechanical stability of materials located at zero pressure.

For the orthorhombic compounds, the criteria is

$$C_{11} + C_{22} - 2C_{12} > 0, \quad C_{11} + C_{33} - 2C_{13} > 0,$$
$$C_{22} + C_{33} - 2C_{23} > 0 \ C_{ii} > 0 \ (i \sim 1-6) \tag{12}$$

$$C_{11} + C_{22} + C_{33} - 2C_{13} + 2C_{12} + C_{13} + 2C_{23} > 0 \tag{13}$$

A significant reliance is placed on elastic constants in the research of crystalline materials [59]. It is possible to establish a connection between nature on a macroscopic size and its qualities on a tiny scale. Hook's law makes use of the relationship that exists between stress and strain to determine elastic constants.

$$\sigma_{ij} = C_{ijkl}\varepsilon_{ij} \tag{14}$$

In the realm of scientific literature, the stiffness matrix symbolized as C_{ijkl} serves as a representation of the elastic constant.

The elasticity of a material can be assessed by examining the behavior of the material's unit cell's minor mechanical strain (δ), as indicated by the elastic constants [60]. In this investigation, we employed the IR-least package established by M. Jamal, derived from the Wien2k code. The model utilized in this study is based on the package above. The functional GGA-PBEsol was employed in this study to estimate the physical property. The elastic constants can be determined by subjecting the material to specific and accurate deformations. The elastic constants reported in the study indicate that the crystal structures of $Ba_4Sb_4Se_{11}$ and $[Ba_4Sb_4Se_{11}]$: Sr^{3+} are highly stable and resistant to deformation. The mechanical

properties can be evaluated by measuring parameters such as Young's modulus, shear modulus, bulk modulus, and Poisson's ratio. The elastic moduli were determined utilizing the Voigt–Reuss–Hill (V_{RH}) methodology [61].

$$B_V = 1/9\left(c_{11} + 2c_{12} + 2c_{13} + c_{22} + 2c_{23} + c_{33}\right) \tag{15}$$

$$B_R = \chi\left[c_{11}\left(c_{22} + c_{33} - 2c_{23}\right) + c_{22}\left(c_{33} - 2c_{13}\right)\right.$$
$$-2c_{33}c_{12} + c_{12}\left(2c_{23} - c_{12}\right) + c_{13}\left(2c_{12} - c_{13}\right)$$
$$\left. + c_{23}\left(2c_{13} - c_{23}\right)\right]^{-1} \tag{16}$$

$$G_V = 1/15\left(c_{11} - c_{12} - c_{13} + c_{22} - c_{23} + c_{33} + 3c_{44} + 3c_{55} + 3c_{66}\right) \tag{17}$$

$$G_R = 15\left\{4[c_{11}\left(c_{22} + c_{33} + c_{23}\right) + c_{22}\left(c_{33} + c_{13} + c_{33}c_{12}\right.\right.$$
$$-c_{12}\left(c_{23} + c_{12}\right) + c_{13}\left(c_{12} + c_{13}\right) - c_{23}\left(c_{13} + c_{23}\right)]/$$
$$\left. \chi + 3\left(c_{44}^{-1} + c_{55}^{-1} + c_{66}^{-1}\right)\right\}^{-1} \tag{18}$$

$$\chi = c_{13}\left(c_{12}c_{23} - c_{13}c_{22}\right) + c_{23}\left(c_{12}c_{13} - c_{23}c_{11}\right) + c_{33}\left(c_{11}c_{22} - c_{12}^2\right) \tag{19}$$

The variables B_V, B_R, G_V, and G_R denote the bulk modulus B and shear modulus boundaries. The bulk and shear moduli calculate the mean value of the computed upper and lower limits. Below is a mathematical formulation representing the bulk modulus (B) and the shear modulus (G).

$$B = \frac{1}{2}\left(B_R + B_V\right) \tag{20}$$

$$G = \frac{1}{2}\left(G_R + G_V\right) \tag{21}$$

The Young modulus E and Poisson's ratio v are based on the calculated values of the bulk modulus B and shear modulus G.

Table 3 elastic constants (C_{ij}, GPa), Zener anisotropy factor (A), bulk modulus (B, GPa), shear modulus (G, GPa), Young's modulus (E, GPa), Poisson's ratio (υ), and B/G ratio for $Ba_4Sb_4Se_{11}$ and $[Ba_4Sb_4Se_{11}]$: Sr^{3+}

Phase	C_{11}	C_{12}	C_{13}	C_{22}	C_{23}	C_{33}	C_{44}	C_{55}	C_{66}
$Ba_4Sb_4Se_{11}$	225.27	104.32	56.32	235.18	70.69	201.32	52.83	45.58	82.50
$[Ba_4Sb_4Se_{11}]$: Sr^{3+}	295.3	140.39	89.98	309.58	95.6	278.80	69.22	69.20	118.55

$$E = \frac{9BG}{3B + G} \tag{22}$$

$$v = \frac{3B - E}{6B} \tag{23}$$

Table presents the values of variables B, G, E, and V. The relationship between the bulk modulus and bond strength is directly proportional, indicating that the bulk modulus is a quantitative indicator of a material's ability to withstand compression within the realm of elasticity. This study investigates the bulk moduli of semiconducting materials. The numerical magnitude of Young's modulus serves as a quantification of the inherent rigidity of a material. The semiconducting material compounds investigated in Table 3 exhibit a consistent trend in the alterations of Young's and shear modulus values. The relationship between Poisson's deformation and stress in an elastic material is a fundamental mechanical property. The equation [62] provides the mathematical expression for determining the value of the Vickers hardness scale.

$$H_V = 0.92(G/B)^{1.3137}G^{0.708} \tag{24}$$

The computed H_V value is shown in Table 3. The chalcopyrite had a similar pattern with the highest Young's modulus E and Vickers hardness H.V. Pugh introduced the B/G ratio as a ductility metric for assessing a material's ductility. Ductility is high when the B/G ratio is high and low when it is low. The material is pliable if the ratio is more than 1.75; if not, it is brittle. The B/G ratios in this analysis indicated the material's flexibility, which was more than 1.75. The correlation between ductility and material concentration was positive. Poisson's ratio (v) has an inverse relationship between bulk and shear modulus. The Poisson's ratio (v) of ductile materials is more significant than 0.26. Their B/G ratio of more than 1.75 and value of more than 0.26 verified the ductility of $Ba_4Sb_4Se_{11}$ and $[Ba_4Sb_4Se_{11}]$: Sr^{3+}

A crucial factor in both engineering science and crystal physics, anisotropy is strongly associated with the potential to create microcracks in materials [63]. Quantifying the directional diversity in atom-to-atom bonding in various crystallographic planes is possible using the shear anisotropic factors. The shear anisotropic factors have been identified for the orthorhombic $Ba_4Sb_4Se_{11}$ and $[Ba_4Sb_4Se_{11}]$: Sr^{3+}. Expressing these shear anisotropic components as anisotropy in elastic materials can be measured by any number less than or equal to one.

Elastic anisotropy is crucial for forecasting a material's fracture stiffness and other critical properties. The elastic anisotropy of material is evaluated using the universal anisotropy index (UAI) and the percent anisotropy indices of compression (A_B) and shear (A_G). These formulas can be used to calculate these indices [64].

$$A^U = 5\frac{G_V}{G_B} + \frac{B_V}{B_R} - 6 \tag{25}$$

$$A_B = \frac{B_V - B_R}{B_V + B_R} \times 100\% \tag{26}$$

$$A_G = \frac{G_V - G_R}{G_V + G_R} \times 100\% \tag{27}$$

The crystal is isotropic if the A_B, A^U, and A_G numerical values are all zero. With every step away from zero, anisotropy increases. In this study, every chalcopyrite exhibits anisotropic behavior. Shear anisotropy is present in the materials but not compression anisotropy, according to the observed values A_B, A_U, and AG H measurements of A^U, A_B, and A_G in $Ba_4Sb_4Se_{11}$ and $[Ba_4Sb_4Se_{11}]$: Sr^{3+} indicate reduced compression and shear anisotropy. Eu's A^U is estimated to be 0.6, indicating a modest level of universal anisotropy. We examined the tangential anisotropy exhibited by the compounds under investigation using the anisotropy factors A_1, A_2, and A_3. The equations for the shear anisotropy factor [63, 64] for tetragonal crystals are as follows:

$$A_1 = \frac{4C_{44}}{C_{11} + C_{33} - 2C_{13}} \tag{28}$$

$$A_2 = \frac{4C_{55}}{C_{22} + C_{33-2C23}} \tag{29}$$

$$A_3 = \frac{4C_{66}}{C_{11} + C_{22-2C12}} \tag{30}$$

The anisotropy of the crystal increased with the difference between the anisotropy factors. The computed values are presented in Table 4. This result suggests that $Ba_4Sb_4Se_{11}$ and $[Ba_4Sb_4Se_{11}]$: Sr^{3+} have the highest shear anisotropy (Table 5).

5 Transport Properties

The semi-classical Boltzmann theory was utilized in the study, and it was incorporated into the Boltztrap code [65]. This was done to evaluate the impact of doping with the composition on the thermoelectric properties of the compounds looked into. An illustration of the Arrhenius plot that describes the relationship between temperature and electrical conductivity in Fig. 15b. It has been shown through empirical research that the base materials $Ba_4Sb_4Se_{11}$ and $[Ba_4Sb_4Se_{11}]$: Sr^{3+} have features typical of semiconductors. The calculated values of Eg for these samples fall between

0.8–4.1 electron volts (eV) most of the time. The result agrees with both compounds' previous measurements and band-structure computations, demonstrating their semiconducting properties. In the context of homogeneous alloys, the temperature changes in electrical conductivity point to a thermally activated behavior with apparent activation energy across the whole temperature range. This behavior occurs regardless of the temperature at which it is seen. The observable semiconducting behavior of homogeneous materials is associated with their significantly high

Table 4 Calculated bulk modulus B, shear modulus G, Young's modulus E, B/G ratio, Poisson ratio ν, and Vickers hardness H_V of $Ba_4Sb_4Se_{11}$ and $[Ba_4Sb_4Se_{11}]$: Sr^{3+}

Phase	B_V	B_R	B	G_V	G_R	G	B/G	E	v	H_V
$Ba_4Sb_4Se_{11}$	99.3	102.2	96.3	81.5	73.2	52.3	3.23	108	0.31	5.2
$[Ba_4Sb_4Se_{11}]$: Sr^{3+}	170.2	285.3	188.3	82.2	89.3	78	2.77	185	0.33	4.58

Table 5 Calculated anisotropic parameters of $Ba_4Sb_4Se_{11}$ and $[Ba_4Sb_4Se_{11}]$: Sr^{3+}

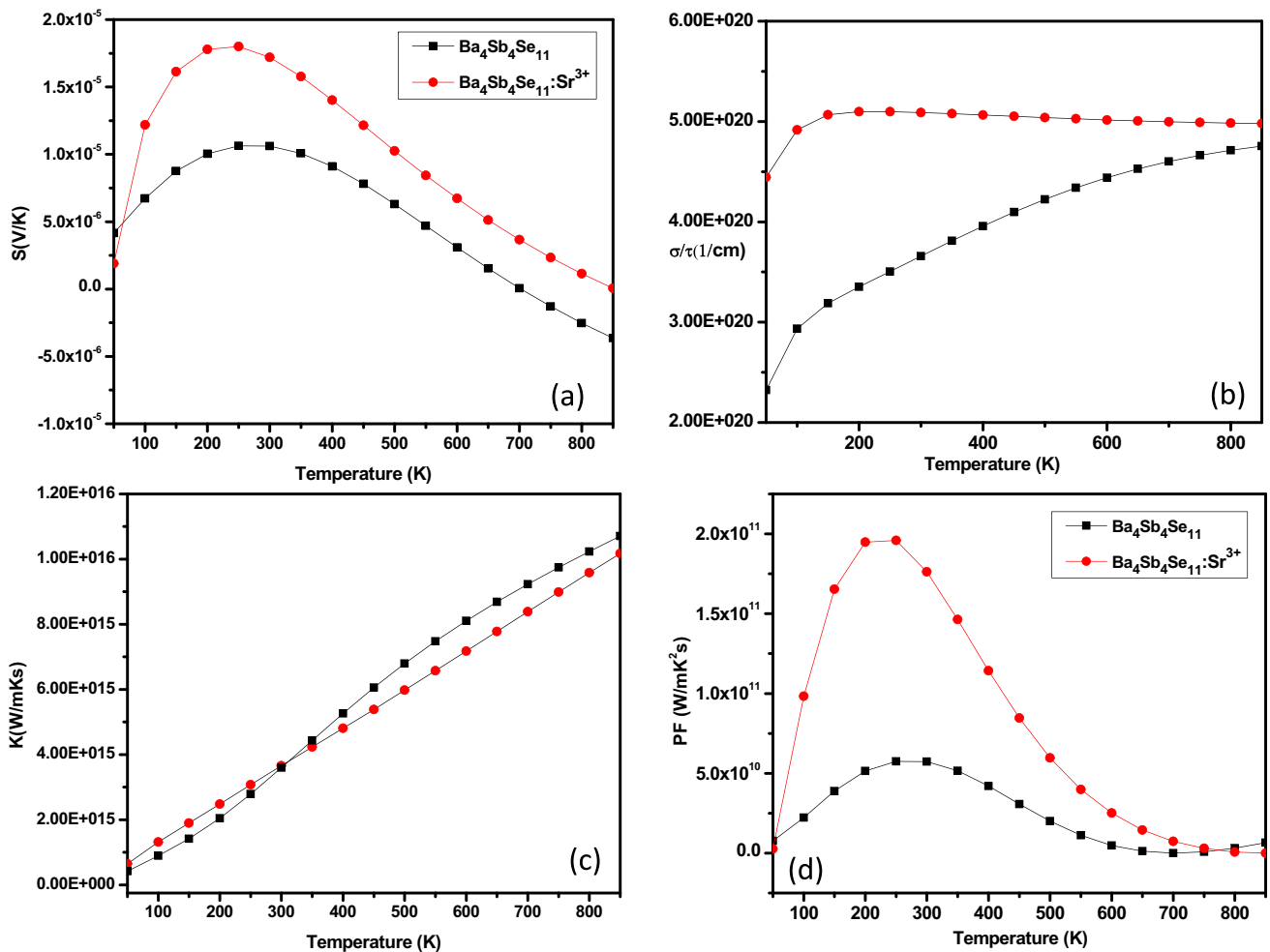| Phase	A^U	A_B	A_G	A_1	A_2	A_3
$Ba_4Sb_4Se_{11}$ $[Ba_4Sb_4Se_{11}]$: Sr^{3+}	2.9	1.88	17.2	3.67	2.8	7.3
	3.8	2.71	15.9	1.20	2.28	8.1

Fig. 15 Calculated **a** Seebeck coefficient,; **b** electrical conductivity, **c** thermal conductivity, **d** power factor of $Ba_4Sb_4Se_{11}$ and $[Ba_4Sb_4Se_{11}]$: Sr^{3+} Selenoantimonate

thermoelectric values, providing further evidence for the observations above. This characteristic is entirely or partially observed, particularly in the high-temperature region. The presence of semiconducting qualities has been suggested to be more likely attributable to structural modifications, such as enhanced ordering within one or more sublattices generated by alloying. This is because structural modifications are more likely to be caused by alloying. The electrical structure is then altered as a result of these structural alterations. This theory is supported by our prior theoretical calculations, which point to the possibility of a band gap in the crystal structure of investigated materials. One of the most important parameters when studying thermoelectric qualities is the Seebeck coefficient, symbolized by the 'S' [66]. To convert energy efficiently, the Seebeck coefficient should have a high absolute value. It should be noted that the Seebeck coefficient can alter with fluctuations and is substantially temperature-dependent. For thermoelectric devices to work efficiently, the electrical conductivity is a measure of a material's capacity to carry electricity must be high. To keep energy losses to a minimum, materials with high electrical conductivity are ideal. Nevertheless, temperature changes can affect electrical conductivity [67]. When a temperature gradient is applied to a material, it measures how much of an increase in the materials thermoelectric voltage is caused by the change. Using the Boltzmann semi-classical transport equation, the Seebeck coefficient 'S', thermal conductivity '(κ_{el})', scattering time 'τ', and electrical conductivity 'σ' were all calculated using the computational code Boltztrap [68, 69]. The tensors of electrical conductivity are found by solving the equation.

$$\sigma_{\alpha,\beta} = e^2 \sum_{i,k} \left[-\frac{\partial f_o(T, \varepsilon, \mu)}{\partial \varepsilon} \right] v_\alpha v_\beta \mathrm{T}_k \tag{31}$$

where $v_\alpha, v_{\beta,} \mathrm{T}_k$ e, α, β, μ e, α, β, μ represent the group velocities, relaxation time, charge on an electron, tensor indices, and chemical potential, respectively. Additionally, f_o denotes the Fermi–Dirac distribution function. The chemical potential (μ) exhibits a range of values defined as $\mu - k_B T < \varepsilon < \mu + k_B T$. The subsequent equation can mathematically describe the distribution of transport.

$$\prod_{i,k} = \sum_{i,k} v_\alpha v_\beta \mathrm{T}_k \tag{32}$$

Among all the coefficients, this one is the most important by far. The thermal conductivity k, electrical conductivity, and Seebeck coefficient S can all be written in the integral representation.

$$k = k_B^2 T \int \prod_{i,k} \left(\frac{\varepsilon - \mu}{k_B T} \right)^2 \left[-\frac{\partial f_o(T, \varepsilon, \mu)}{\partial \varepsilon} \right] d\varepsilon \tag{33}$$

$$\sigma = e^2 \int \prod_{i,k} \left[-\frac{\partial f_o(T, \varepsilon, \mu)}{\partial \varepsilon} \right] d\varepsilon \tag{34}$$

Disparities are clearly visible; in particular both investigated materials studied have thermal conductivities [70] around 0.6×10^{15} (W/mKs), which is comparable to the conductivities of other materials of a similar order of magnitude. However, the thermal conductivity at 800 K (1.2×10^{16} (W/mKs) is significantly higher. The increased electronic contribution to thermal conductivity may account for the observed discrepancy and the typically enhanced conductivities of heterogeneous materials compared to the other samples. A more significant concentration of current carriers caused by point defects and secondary phases is probably to blame for this boost. The effect of electronic contribution on thermal conductivity can be understood using the Wiedemann–Franz–Lorenz law. The size of a material's band gap is a significant factor in establishing its electrical properties. The band gap determines the thermal and electrical conductivities and the Fermi energy can be used as a rough approximation for the electrical conductivity and the Seebeck coefficient.

It should be noted that the phonon contribution to thermal conductivity is not included in the Boltztrap code. The effective mass is proportional to the Seebeck coefficient; therefore, if the band energy shifts, so will the effective mass. An increase in charge mobility and the Seebeck coefficient results from forming dense and flat energy bands at the Fermi energy. Electric conductivity also rises with a rise in charge mobility and the Seebeck coefficient. ZT is an equation used to calculate a material's thermoelectric efficiency [66, 70, 71].

The ZT equation is expressed as

$$ZT = \sigma S^2 / \kappa T \tag{35}$$

It is evident from the equation that the thermoelectric efficiency (ZT) demonstrates a direct relationship with the variables "σ, T, and S^2" while showing an inverse relationship with the variable "k". For thermoelectric materials to be used in the real world, keeping a few things in mind is crucial. Important factors include the difference between the bulk and surface values of the electrical conductivity-to-relaxation-time ratio, the Seebeck coefficient, and the thermal conductivity-to-relaxation-time ratio near the Fermi energy level. The presence of flat and dense energy bands further aids higher carrier concentration. An increase in temperature and the electrical conductivities of 5.2×10^{20} (cm)$^{-1}$, $4.5.0 \times 10^{20}$ (cm)$^{-1}$, and 5.6×10^{20} (cm)$^{-1}$ are observed in materials with the formula $Ba_4Sb_4Se_{11}$ and $[Ba_4Sb_4Se_{11}]$: Sr^{3+}. The rate at which heat travels through a conductor as the temperature gradient between the material and its surroundings

Table 6 Calculated thermoelectric properties of $Ba_4Sb_4Se_{11}$ and $[Ba_4Sb_4Se_{11}]$: Sr^{3+}

Compound	(κ) (W/Kms)	(σ/τ) (Ωms)$^{-1}$	PF (W/mK^{2}s)	S (V/K)
$Ba_4Sb_4Se_{11}$	0.98×10^{16}	6.0×10^{20}	4.0×10^{10}	1.0×10^{-8}
$[Ba_4Sb_4Se_{11}]$: Sr^{3+}	0.97×10^{16}	7.0×10^{20}	2.2×10^{11}	1.9×10^{-8}

changes is defined as the electrical and thermal conductivity of the material. Lattice vibrations and free electrons are typically responsible for a material's heat conductivity. The lattice and electronic components determine the overall thermal conductivity, which varies with temperature uniquely, as indicated in Fig. 15c. Seebeck coefficient S results in a greater concentration of charge carriers [71]. Figure 15a shows the Seebeck coefficient plot and the results of the Boltztrap code. It is observed that both materials are P-type upto 700 K, while on increasing temperature, their nature changed to n-type. An abundance of electrons, denoted by this negative number, indicates the presence of n-type carriers. The S exhibits a sharp decline with increasing temperature, with a maximum value at 100 K (1.5×10^{-5} V K^{-1}) and a minimum at 800 K; from 150 to 800 K, the S values of and $[Ba_4Sb_4Se_{11}]$: Sr^{3+} are negative. There is proof of n-type carriers and obligations to this observation. Positive trends in the Seebeck coefficients indicate that the other $Ba_4Sb_4Se_{11}$ and $[Ba_4Sb_4Se_{11}]$: Sr^{3+} and the parent material are p-type. At a temperature of 100 K, the Seebeck coefficient is between its maximum positive values of (1.95×10^{-6} V K^{-1}) and (1.3×10^{-5} V K^{-1}). The Seebeck coefficient then drops as the temperature is raised to about 300 K. Figure 15a depicts typical semiconductor behavior, which includes a reduction in electrical conductivity with increasing temperature for both compounds and a linear increase for doped materials. $Ba_4Sb_4Se_{11}$ has a power factor of negligible until a temperature of about 50 K. Then, while the temperature keeps climbing, there is a sudden jump in the power factor. At a temperature of 250 K, it reaches its maximum value of 2.0×10^{11} W m^{-2} s^{-1}. The power factor of Sr doped compound increased compared to other concentrations due to substituting 0.05 atoms with Sr^{3+}. At a temperature of 250 K, the power factor is at its maximum of between 0.0 and 1.5 0×10^{10} W m^{-1} K^{-2} s^{-1}. However, the power factor rapidly declines when the temperature increases and eventually hits zero, getting above 352 K, and the power factor rises steadily alongside the temperature as shown in Fig. 15d (Table 6).

6 Conclusions

We provide here the findings of an exhaustive study investigating the mechanical, electrical, optical, and structural characteristics of $Ba_4Sb_4Se_{11}$ and $[Ba_4Sb_4Se_{11}]$: Sr^{3+}

Selenoantimonate using first-principles methods. Among the many parameters measured in this study are the extinction coefficient, the absorption coefficient, the reflectivity, the refractive index, the optical conductivity, and the birefringes. The bulk modulus, shear modulus, Young's modulus, and Poisson's ratio are elastic parameters computed concerning mechanical stability and anisotropic sound velocities. The investigated compounds exhibit semiconductor characteristics according to the energy band dispersion results. Specifically in the visible range, these compounds' band gaps are between 2.2 and 1.68 eV. Finding the sources of the electronic states that make up the energy bands is done using Partial Density of States (PDOS) diagrams. In the energy range of 0 eV to 14 eV, frequency-dependent linear optical properties are calculated for the Selenoantimonate that was studied. Because birefringence is highly valued over a wide frequency range, phase-matching skills are ensured. Results from the experiments suggest that the compounds under study have positive characteristics that make them promising candidates for use in thermoelectric applications. These compounds show promise as optoelectronic industry solar cell and LED source materials. The transport properties are estimated using the principles of Boltzmann transport theory. Assessing the Seebeck coefficient, electrical conductivity, thermal conductivity, and power factor involves utilizing the Boltzmann transport theory. The enhanced thermoelectric performance of the studied $Ba_4Sb_4Se_{11}$ and $[Ba_4Sb_4Se_{11}]$: Sr^{3+} Selenoantimonate is achieved through the increased mobility of carriers, resulting in improved thermoelectric efficiency. Our results will serve as a valuable guide for future experimental and commercial applications.

Declarations

Ethical Approval We, the undersigned, declare that this manuscript is original, has not been published before, and is not currently being considered for publication elsewhere. We confirm that the manuscript has been read and approved by all named authors and that there are no other persons who satisfied the criteria for authorship but are not listed. We further confirm that all have agreed on the order of authors listed in the manuscript us.

References

1. G. Cordier, R. Cook, H. Schäfer, Novel selenoantimonate (iii) anions in $Ba_4Sb_4Se_{11}$. Angew. Chem. Int. Ed. Engl. **19**(4), 324–325 (1980)

2. A. Manongdo, Facile amine-surfactant thermal syntheses, structures, and properties of novel crystalline silver thioantimonates (2017)

3. Z. Huang et al., A sulfur-doped carbon-enhanced $Na_3V_2(PO_4)_3$ nanocomposite for sodium-ion storage. J. Phys. Chem. Solids **167**, 110746 (2022)

4. Z. Huang et al., Constructing one-dimensional mesoporous carbon nanofibers loaded with $NaTi_2(PO_4)_3$ nanodots as novel anodes for sodium energy storage. J. Phys. Chem. Solids **161**, 110479 (2022)

5. X.-F. Chen, Periodic density functional theory (PDFT) simulating crystal structures with microporous CHA framework: an accuracy and efficiency study. Inorganics **11**(5), 215 (2023)

6. H. Schnöckel, Matrix isolation of OSiS: IR spectroscopic evidence for the Si=S double bond. Angew. Chem. Int. Ed. Engl. **19**(4), 323–324 (1980)

7. S.A. Vaselabadi et al., Scalable synthesis of selenide solid-state electrolytes for sodium-ion batteries. Inorg. Chem. **62**(42), 17102–17114 (2023)

8. X. Chen, T. Yu, Simulating crystal structure, acidity, proton distribution, and IR spectra of acid zeolite HSAPO-34: a high accuracy study. Molecules **28**(24), 8087 (2023)

9. S. Ye et al., Design strategies for perovskite-type high-entropy oxides with applications in optics. ACS Appl. Mater. Interfaces. **15**(40), 47475–47486 (2023)

10. L. Pan et al., Reassessing self-healing in metallized film capacitors: a focus on safety and damage analysis. IEEE Trans. Dielectr. Electr. Insul. (2024). https://doi.org/10.1109/TDEI.2024.3357441

11. I. Hadar et al., Modern processing and insights on selenium solar cells: the world's first photovoltaic device. Adv. Energy Mater. **9**(16), 1802766 (2019)

12. B.J. Stanbery, Copper indium selenides and related materials for photovoltaic devices. Crit. Rev. Solid State Mater. Sci. **27**(2), 73–117 (2002)

13. J. Guo et al., Resurrected and tunable conductivity and ferromagnetism in the secondary growth $La_{0.7}Ca_{0.3}MnO_3$ on transferred $SrTiO_3$ membranes. Nano Lett. **24**, 1114 (2024)

14. Z. Wang et al., Improvement of electron transfer efficiency during denitrification process by Fe-Pd/multi-walled carbon nanotubes: possessed redox characteristics and secreted endogenous electron mediator. Sci. Total Environ. **781**, 146686 (2021)

15. Z.-Z. Luo et al., Extraordinary role of Zn in enhancing thermoelectric performance of Ga-doped n-type PbTe. Energy Environ. Sci. **15**(1), 368–375 (2022)

16. Y. Wu et al., Metastable structures with composition fluctuation in cuprate superconducting films grown by transient liquid-phase assisted ultra-fast heteroepitaxy. Mater. Today Nano **24**, 100429 (2023)

17. Y. Lu et al., Mixed-mode operation of hybrid phase-change nanophotonic circuits. Nano Lett. **17**(1), 150–155 (2017)

18. Z. Huang et al., Improved electrical resistivity-temperature characteristics of oriented hBN composites for inhibiting temperature-dependence DC surface breakdown. Appl. Phys. Lett. (2023). https://doi.org/10.1063/5.0166638(10)

19. A. Kertman, N. Shal'neva, Phase equilibria in the $BaS–Ga_2S_3$ system. Russ. J. Inorg. Chem. **61**, 109–114 (2016)

20. P. Mukdeeprom-Burckel, J.G. Edwards, Chemistry and thermodynamics of solid and vapor phases in the barium-sulfide, gallium-sulfide system. Mater. Res. Bull. **25**(2), 163–172 (1990)

21. M.R. Davolos et al., Luminescence of Eu^{2+} in strontium and barium thiogallates. J. Solid State Chem. **83**(2), 316–323 (1989)

22. L. Sokolovskaya, S. Kvyatkovskiy, A. Semenova, Barite phase formations during lead and zinc oxidized ores sintering. Integr. Min. Raw Mater. **1**, 304 (2018)

23. H.A. Petersen et al., Electrochemical methods for materials recycling. Mater. Adv. **2**(4), 1113–1138 (2021)

24. M.A. Shah et al., Applications of nanotechnology in smart textile industry: a critical review. J. Adv. Res. **38**, 55–75 (2022)

25. R. Arvidsson, B.A. Sandén, Carbon nanomaterials as potential substitutes for scarce metals. J. Clean. Prod. **156**, 253–261 (2017)

26. J. Zhu et al., An overview of the engineered graphene nanostructures and nanocomposites. RSC Adv. **3**(45), 22790–22824 (2013)

27. P.I. Dolez, Nanomaterials definitions, classifications, and applications, in *Nanoengineering*. (Elsevier, Amsterdam, 2015), pp.3–40

28. X. Feng et al., Construction of CdS@ ZnO core–shell nanorod arrays by atomic layer deposition for efficient photoelectrochemical H_2 evolution. Sep. Purif. Technol. **324**, 124520 (2023)

29. Y. Zhang et al., Tuning the red-to-green-upconversion luminescence intensity ratio of Na_3ScF_6: 20% Yb^{3+}, 2% Er^{3+} particles by changes in size. Materials **16**(6), 2247 (2023)

30. M.S. Khan et al., Tailoring the optoelectronic, thermoelectric, and thermodynamic properties of rare-earth quaternary chalcogenides: an inclusive first-principles study. Mater. Today Commun. **38**, 107848 (2024)

31. D. Liu et al., Alloy engineering to tune the optoelectronic properties and photovoltaic performance for Hf-based chalcogenide perovskites. Mater. Sci. Semicond. Process. **169**, 107919 (2024)

32. S. Goumri-Said et al., Unraveling essential optoelectronic and thermoelectric excellence in $CsZrCuSe_3$ with hybrid functional and Boltzmann transport insights. Res. Phys. **57**, 107395 (2024)

33. B. Zhang et al., Determination and assessment of a complete and self-consistent electron-neutral collision cross-section set for the C4F7N molecule. J. Phys. D Appl. Phys. **56**(13), 134001 (2023)

34. X. Song et al., Control of the electron dynamics in solid-state high harmonic generation on ultrafast time scales by a polarization-skewed laser pulse. Opt. Express **31**(12), 18862–18870 (2023)

35. X. Liu, L. Zhang, J. Wang, Design strategies for MOF-derived porous functional materials: preserving surfaces and nurturing pores. J. Materiomics **7**(3), 440–459 (2021)

36. M. Kalaj et al., MOF-polymer hybrid materials: from simple composites to tailored architectures. Chem. Rev. **120**(16), 8267–8302 (2020)

37. T. Wu, J. Wang, Global discovery of stable and non-toxic hybrid organic-inorganic perovskites for photovoltaic systems by combining machine learning method with first principle calculations. Nano Energy **66**, 104070 (2019)

38. S. Dahbi et al., Importance of spin-orbit coupling on photovoltaic properties of Pb-free vacancy ordered double perovskites halides X2TeY6 (X= Cs, Rb, and Y= I, Br, Cl): first-principles calculations. Int. J. Energy Res. **46**(6), 8433–8442 (2022)

39. P. Kumari et al., A first-principles prediction of thermophysical and thermoelectric performances of $SrCeO_3$ perovskite. Int. J. Energy Res. **46**(3), 2934–2946 (2022)

40. D. Hoat, J.R. Silva, A.M. Blas, First principles study on structural, electronic and optical properties of Ga1− xBxP ternary alloys (x= 0, 0.25, 0.5, 0.75 and 1). Phys. Lett. A **382**(29), 1942–1949 (2018)

41. M.N. Rasul et al., DFT based structural, electronic and optical properties of B1−xInxP (x= 0.0, 0.25, 0.5, 0.75, 1.0) compounds: PBE-GGA vs. mBJ-approaches. Chin. J. Phys. **56**(6), 2659–2672 (2018)

42. A. Radzwan et al., First-principles calculations of the stibnite at the level of modified Becke–Johnson exchange potential. Chin. J. Phys. **56**(3), 1331–1344 (2018)

43. G.J. Snyder, T.S. Ursell, Thermoelectric efficiency and compatibility. Phys. Rev. Lett. **91**(14), 148301 (2003)

44. M. Blanco, E. Francisco, V. Luana, GIBBS: isothermal-isobaric thermodynamics of solids from energy curves using a quasi-harmonic Debye model. Comput. Phys. Commun. **158**(1), 57–72 (2004)

45. V. Milman, M. Warren, Elastic properties of TiB_2 and MgB_2. J. Phys.: Condens. Matter **13**(24), 5585 (2001)

46. A.A. Emery, C. Wolverton, High-throughput DFT calculations of formation energy, stability and oxygen vacancy formation energy of ABO3 perovskites. Sci. Data **4**(1), 1–10 (2017)

47. S. Jana et al., Extremely low thermal conductivity in BaSb2Se4: Synthesis, characterization, and DFT studies. J. Solid State Chem. **315**, 123524 (2022)

48. D. Mei et al., Syntheses and characterization of two new selenides Ba5Al2Se8 and Ba5Ga2Se8. J. Alloy. Compd. **509**(6), 2981–2985 (2011)

49. C.F. Bohren, D.R. Huffman, *Absorption and scattering of light by small particles* (Wiley, Hoboken, 2008)

50. F. Gervais, Optical conductivity of oxides. Mater. Sci. Eng. R. Rep. **39**(2–3), 29–92 (2002)

51. Q. Zhang et al., An all-organic composite actuator material with a high dielectric constant. Nature **419**(6904), 284–287 (2002)

52. L.B. Wolff, Polarization-based material classification from specular reflection. IEEE Trans. Pattern Anal. Mach. Intell. **12**(11), 1059–1071 (1990)

53 R.F. Egerton, *Electron energy-loss spectroscopy in the electron microscope* (Springer, Cham, 2011)

54. I. Liberal, N. Engheta, How does light behave in a material whose refractive index vanishes? Phys. Today **75**(3), 62–63 (2022)

55. D. Kuang et al., High molar extinction coefficient heteroleptic ruthenium complexes for thin film dye-sensitized solar cells. J. Am. Chem. Soc. **128**(12), 4146–4154 (2006)

56. D.O. Dorohoi et al., Review on optical methods used to characterize the linear birefringence of polymer materials for various applications. Molecules **28**(7), 2955 (2023)

57. J. Gosline et al., Elastic proteins: biological roles and mechanical properties. Philos. Trans. Royal Soc. Lond. Ser. B Biol. Sci. **357**(1418), 121–132 (2002)

58. J. Pokluda et al., Ab initio calculations of mechanical properties: methods and applications. Prog. Mater Sci. **73**, 127–158 (2015)

59. R. Hearmon, The elastic constants of anisotropic materials—II. Adv. Phys. **5**(19), 323–382 (1956)

60. E. Ptochos, G. Labeas, Elastic modulus and Poisson's ratio determination of micro-lattice cellular structures by analytical, numerical and homogenisation methods. J. Sandwich Struct. Mater. **14**(5), 597–626 (2012)

61. Y. Luo, Isotropized Voigt-Reuss model for prediction of elastic properties of particulate composites. Mech. Adv. Mater. Struct. **29**(25), 3934–3941 (2022)

62. E. Broitman, Indentation hardness measurements at macro-, micro-, and nanoscale: a critical overview. Tribol. Lett. **65**(1), 23 (2017)

63. C. Sweeney et al., The role of elastic anisotropy, length scale and crystallographic slip in fatigue crack nucleation. J. Mech. Phys. Solids **61**(5), 1224–1240 (2013)

64. Y. Duan et al., Anisotropic elastic properties of the Ca–Pb compounds. J. Alloy. Compd. **595**, 14–21 (2014)

65. G.K. Madsen, J. Carrete, M.J. Verstraete, BoltzTraP2, a program for interpolating band structures and calculating semi-classical transport coefficients. Comput. Phys. Commun. **231**, 140–145 (2018)

66. O. García et al., Single phase power factor correction: a survey. IEEE Trans. Power Electron. **18**(3), 749–755 (2003)

67. M. Irfan et al., Fe and Rh doping nanoarchitectonics on properties of Sr2YGaX2O7 pyrochlore oxides with a DFT-based spin-polarized calculation for optoelectronic and thermoelectric applications. J. Inorg. Organomet. Polym. Mater. (2023). https://doi.org/10.1007/s10904-023-02845-z

68 N. Neophytou, *Theory and simulation methods for electronic and phononic transport in thermoelectric materials* (Springer, Cham, 2020)

69. G. Naydenov et al., Effective modelling of the Seebeck coefficient of Fe_2VAl. J. Phys.: Condens. Matter **32**(12), 125401 (2019)

70. O. Garcia et al., Power factor correction: a survey. In 2001 IEEE 32nd annual power electronics specialists conference (IEEE Cat. No. 01CH37230). IEEE (2001)

71. X. Guan, J. Ouyang, Enhancement of the Seebeck coefficient of organic thermoelectric materials via energy filtering of charge carriers. CCS Chem. **3**(10), 2415–2427 (2021)